Analyst

Accepted Manuscript

ROYAL SOCIETY OF CHEMISTRY

www.rsc.org/analyst

Cite this: DOI: 10.1039/c0xx00000x

www.rsc.org/xxxxxx

ARTICLE TYPE

Dielectrophoretic isolation of cells using 3D microelectrodes featuring castellated blocks

Xiaoxing Xing and Levent Yobas*[a]

Received (in XXX, XXX) Xth XXXXXXXXX 20XX, Accepted Xth XXXXXXXXX 20XX

DOI: 10.1039/b000000x

We present 3D microelectrodes featuring castellated blocks for dielectrophoretically isolating cells. These electrodes provide a more effective dielectrophoretic force field than thin-film surface electrodes and yet immobilize cells near stagnation points across a parabolic flow profile for enhanced cell viability and separation efficiency. Unlike known volumetric electrodes with linear profiles, the electrodes with structural variations introduced along their depth scale are versatile for constructing monolithic structures with readily integrated fluidic paths. This is exemplified here in the design of an interdigitated comb array wherein electrodes with castellated surfaces serve as building blocks and form digits with an array of fluidic pores. Activation of the design with low-voltage oscillations (±5 V_p, 400 kHz) is found adequate for retaining most viable cells (90.2% ± 3.5%) while removing nonviable cells (88.5% ± 5%) at an increased throughput (5×10^5 cells h^{-1}). The electrodes, despite their intricate profile, are structured into single-crystal silicon through a self-aligned etching process without a precision layer-by-layer assembly.

Introduction

The isolation of a specific cell type from a given complex sample is a daunting task but of a great significance in many practical applications from clinical specimen analysis to water and food quality monitoring. While bulk laboratory techniques such as centrifugation or filtration work well for preparative steps or high-throughput applications, more demanding tasks requiring high purity or high recovery from rare samples call for high-resolution efficient techniques. Techniques such as flow cytometry or fluorescence-activated cell sorting (FACS), despite being capable of addressing this need, are specific to extrinsic labels, and involve bulky and costly instruments run by highly skilled staff.

Dielectrophoresis or DEP is the phenomenon identified with the motion of polarizable particles in suspension due to net columbic force acting on their induced dipole moment in a spatially inhomogeneous alternating electric field.[1,2] The technique, because of its potential for high-resolution cell separation in microfluidics, has gained tremendous momentum among the research community with the advent of miniaturization.[3–5] Moreover, DEP is free of labels and specific to dielectric nature of cells with respect to that of immersion medium, both being a complex function of the applied field frequency. At a particular frequency, cells that are more polarizable than the immersion medium are attracted toward nearest field maxima (positive DEP, i.e. pDEP) while those that are less polarizable are repelled from such regions (negative DEP, i.e. nDEP), hence becoming spatially separated based on their dielectric signature. At a so-called crossover frequency, cells and the medium are equally polarizable such that the DEP force field is nullified.

DEP has been demonstrated to date for numerous applications involving various bioparticles. It has been utilized to separate platelets,[6] cancer cells,[7,8] stem cells,[9] and yeast,[10] from blood, viable yeast[11] and mammalian cells[12] from nonviable cells, bacteria[13,14] and virus particles[15] from yeast or their mixtures, as well as separate malignant cells[16] from healthy breast cells. It has also been applied to align and manipulate organelles,[17] detect parasites,[18] transport blood,[19] and study dielectric properties of various cell types.[20–22] Moreover, physiologic or pathologic changes in cells have been evaluated in response to parasite infection,[23] transfection,[24] drug agents,[25] and the agents that induce multidrug resistance reversal,[26] cell division cycle,[27] cytotoxicity[28] or apoptosis.[29,30] Furthermore, handling, positioning, or patterning of individual cells has been demonstrated for their imaging and sorting,[31,32] electrochemical assays[33] and selective electroporation.[34]

In many applications, the spatially inhomogeneous electric field is often induced by means of thin-film surface microelectrodes lithographically patterned in various configurations with the castellated,[11,15,35] interdigitated,[14,36] and polynomial designs[14,15] arguably among the most popular. DEP has also been paired with other techniques such as steric or gravitational field flow fractionation (FFF) to counterbalance the force fields for a more specific cell separation.[37,38] Since the DEP force field quickly wears off away from the electrodes in a quasi-2D formation, 3D designs have gained more and more

importance despite their demanding integration process.[39–47] For instance, thin-film electrodes placed on the chamber top and bottom walls require careful alignment during assembly whereas those placed on the sidewalls face the issue of lithographic patterning.[39–42] Forming the sidewalls out of volumetric electrodes such as doped silicon mesas through etching,[43,44] extruded metals through electroplating,[45,46] or an array of carbon posts through resist pyrolysis[47] often needs multiple layers of photolithography to route electrical leads to the isolated electrode parts as well as to establish the required fluidic isolation. In particular, metal electroplating and resist pyrolysis involve thick-film lithography that limits the minimum possible spacing between the electrodes. Resist pyrolysis further leads to shrinkage that brings dimensional inconsistencies across the carbon posts. More importantly, none of these methods takes advantage of the wall profiles; uniform straight walls not only lack the ability to tune the DEP force field across the channel depth but also deprive the electrodes of a genuine 3D profile, the presence of which could ease the overall integration. Only recently, have researchers begun to explore 3D electrodes with curved walls by introducing novel process techniques.[48,49]

We have developed 3D electrodes with castellated blocks that bring immediate advantage to their electrical and fluidic integration. Such design allows for electrode segments placed across the flow chamber without interrupting the flow and yet retain a monolithic construct that is electrically intact (a good analogy exists in the architecture of a pier structure). This renders the additional interconnecting layer for electrical continuity redundant. Leveraging this unique profile, we have built an interdigitated 3D comb array as described schematically in Fig. 1. The digits consist of repeating units of electrodes with their castellated surfaces giving rise to an array of round pores. The digits extend nearly fully, thereby partitioning the chamber into equal compartments and, with the pores coaxially aligned, maintain a laminar flow pattern that leaves stagnation points coincide with cell trapping sites under pDEP. Similarly, the castellated surface profile holds such sites towards the chamber top and bottom where the fluid velocity and shear stress are relatively low across a pressure-driven parabolic flow profile. This offers the possibility of using increased flow rates and/or reduced voltages without the risk of compromising cells retained under pDEP, which is beneficial for high throughput applications. The design is validated here by separating viable and nonviable cells. The use of a viable/nonviable separation model for the presented design is a step toward extending the potential use of such 3D electrode profile in various other configurations for biomedical applications.

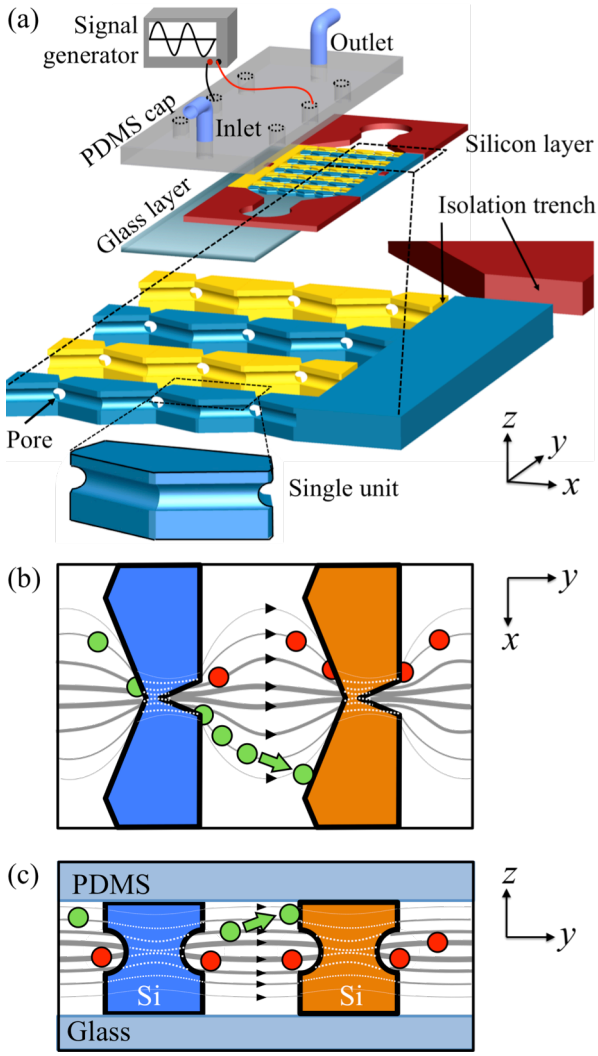

Fig. 1 Illustrations of an interdigitated 3D comb array where the electrode digits consist of repeating units featuring castellated blocks. (a) Exploded view: electrodes structured in doped silicon (blue and yellow) sandwiched between a glass substrate and an elastomer cover. The electrodes and inactive silicon blocks (red) are kept apart by isolation trenches. The castellations lead to a uniform array of pores along the digits while retaining electrical continuity. The castellations and coaxially arranged pores align cell trapping sites near stagnation points in pressure-driven flow as described in the illustrations outlining an electrode pair in (b) planar and (c) cross-sectional views. Cells held under pDEP (light balls) encounter minimal shear (thin streamlines) while other cells (dark balls) are removed by an effective flow (thick streamlines).

Theory

According to the dipole moment method, the time-averaged DEP force $\langle \mathbf{F}_{DEP} \rangle$ acting on a spherical cell with radius R immersed in a medium with dielectric constant ε_m and a spatially non-uniform background electric field vector $\mathbf{E}$ can be expressed as:[1]

$$\langle \mathbf{F}_{DEP} \rangle = \pi \varepsilon_m R^3 \mathrm{Re}[f_{CM}(\omega)] \nabla \left(\tilde{\mathbf{E}} \cdot \tilde{\mathbf{E}}^* \right) \quad (1)$$

where $\tilde{\mathbf{E}}$ is the phasor amplitude of the electric field vector, i.e., $\mathbf{E} = Re\left(\tilde{\mathbf{E}} e^{j\omega t}\right)$, $\omega = 2\pi f$ is the angular frequency with f being the temporal frequency of the applied field, $*$ is the complex conjugate operator, and $\mathrm{Re}[f_{CM}(\omega)]$ is the real part of the complex, frequency-dependent Claussius-Mossotti (CM) factor which is defined in terms of the complex permittivity of cells $\tilde{\varepsilon}_{cell}$ and of the medium $\tilde{\varepsilon}_m$ through:

$$f_{CM}(\omega) = \frac{\tilde{\varepsilon}_{cell} - \tilde{\varepsilon}_m}{\tilde{\varepsilon}_{cell} + 2\tilde{\varepsilon}_m} \quad (2)$$

The complex permittivity $\tilde{\varepsilon}_i$ is given by:

$$\tilde{\varepsilon}_i = \varepsilon_i + \sigma_i / j\omega \quad (3)$$

where ε_i and σ_i are the absolute permittivity and absolute conductivity of the spatial domain denoted by the subscript i (*e.g.*, cell, medium) and $j = \sqrt{-1}$. The dielectric properties of viable cells are approximated by a single-shell model (see ESI).

Cells in a medium of constant flow velocity $\mathbf{\upsilon}_m$ and viscosity η, when subjected to a non-uniform electric field, could reach terminal velocity $\mathbf{\upsilon}_{cell}$ at the equilibrium of the drag and DEP forces:[50]

$$\mathbf{\upsilon}_{cell} = \mathbf{\upsilon}_m + \mu_{DEP}\nabla\left(\tilde{\mathbf{E}} \cdot \tilde{\mathbf{E}}^*\right) \quad (4)$$

where the dielectrophoretic mobility is defined as $\mu_{DEP} = (\varepsilon_m R^2/6\eta)\mathrm{Re}[f_{CM}(\omega)]$.

Methods and materials

Cells and reagents

Human colorectal carcinoma cells (HCT116, ATCC) were cultured in Dulbecco's modified Eagle medium (DMEM) supplemented with 10% fetal bovine serum (FBS) and incubated with 5% CO_2 environment at 37 °C. Pluronic F-68 (0.05%, GE Healthcare Lifescience, Inc.) was added to culture medium to enhance the membrane stability. Cells, before being detached from culture dishes with trypsin–EDTA treatment, were washed with phosphate-buffered saline (PBS) solution and subsequently after being detached suspended in original culture medium. Solutions used in the experiments were passed through a 0.22-μm membrane filter.

Harvested cells were divided into two batches to prepare live and dead cell samples. Dead cells were prepared by heating one of the batches in 65 °C water bath for about 15 min. Then live and dead cells were, respectively, stained with 2 μg/mL Calcein AM (Life Technologies, Inc.) and 50 μg/mL propidium iodide (PI, Sigma-Aldrich). Afterwards, cells were washed twice in DEP buffer (300 mM D-Mannitol) at $100g$ for 5 min, and the subsequent cell pellets of live and dead cells were mixed in DEP buffer at an equal cell density of 10^6 /mL. The conductivity of DEP buffer was measured by a meter (Mettler-Toledo, SevenGo Duo pro) and tuned to the required level by using PBS solution.

Measurements

Prior to each experiment, the device was coated with 5% BSA in DEP buffer for 30 min and then preconditioned with the same buffer to minimize cell adhesion to the chamber surface. The inlet port was connected to a 1 mL syringe (BD Tuberculin) to inject the sample through a syringe pump (Harvard Apparatus). Throughout the sample injection, the device was kept active with a continuous sine-wave voltage monitored on an oscilloscope (Tektronix TDS 2012C) while being supplied from a function generator (Tektronix CFG250) through an amplification unit involving a transformer and a power amplifier (Amp-Line Corp., NY, AL-50HFA). An epi-fluorescence microscope (Nikon Eclipse, FN1) equipped with CCD (RT3Mono, SPOT) was utilized to observe the device. During the entire experiment, a sequence of still images focusing on the device outlet was captured and then analyzed to enumerate viable cells that escaped (positive for Calcein-AM). Upon depleting the sample, a sequence of images was also captured while scanning the entire flow chamber to enumerate nonviable cells being trapped (positive for PI). Based on the cells enumerated and the initial density of the either subpopulation, the viable cells retained and nonviable cells removed were evaluated and then normalized with respect to their initial density to obtain capture and removal statistics.

Computations

All the computations were performed in COMSOL Multiphysics Software 3.5 (Comsol Inc., MA). For viable and nonviable cells, MATLAB (The Mathworks Inc., MA) was utilized to evaluate and plot the real part of the Claussius-Mossotti (CM) factor $\mathrm{Re}[f_{CM}(\omega)]$ according to a single-shell model described in ESI.

Devices

The interdigitated 3D comb array with castellated blocks was conveniently fabricated here in doped silicon crystal using a self-aligned etching technique based on tailoring the depth profile through a sequence of deep reactive ion etch (DRIE) and isotropic etch steps (ESI).[51-53]

Results and discussion

Design

Fig. 2a depicts a representative device without the cover plate. The interdigitated 3D comb array electrodes serve as the active walls of a transparent flow chamber (3 mm wide and 9 mm long) and are isolated from the non-active walls surrounding the inlet/outlet ports through four trenches. Each isolation trench is 100 μm wide and sealed with an insulating PDMS plug cured *in situ*, Fig. 2b. Fig. 2c depicts cells imaged in the transparent device showing the device compatibility with differential interference contrast (DIC) microscopy. The electrode digits (15 pairs) with each consisting of identical electrode units featuring a castellated depth profile cut across the flow chamber contributing uniformly spaced 10 identical pores per digit. Thus, the entire chamber is populated with an array of 300 pores that can be electrically activated.

Each of the pores measures 60 μm in nominal diameter, which can be tuned by adjusting isotropic etch duration. Figs. 2d and e reveal the pores and the 3D castellated profile of the electrode digits in SEM images. As seen, the segments above and below the pores exhibit characteristic DRIE profile and measure about 30 and 110 μm thick, respectively. The pores are coaxially aligned to permeate the laminar flow streams orthogonally through the digits. The digits are physically segregated from the main body of the counter electrode through 10-μm isolation gaps, Fig. 2b.

Simulation

Fig. 3 reveals heat maps of the electric field intensity, the flow velocity, and the shear rate numerically modeled for the 3D comb array (ESI). The electric field intensity maps also present DEP force vectors. In simulations, electrical and fluidic boundary conditions were set at ±5 V_p 400 kHz, and 116 μm/s, respectively. The latter corresponds to maximum flow rate applied in experiments (0.25 mL/h). The aqueous buffer solution was assumed at a conductivity of 100 μS/cm. Maps in upper panel signify the device plane bisecting the upper DRIE segments (15 μm below the cover plate). Maps in middle and lower panel

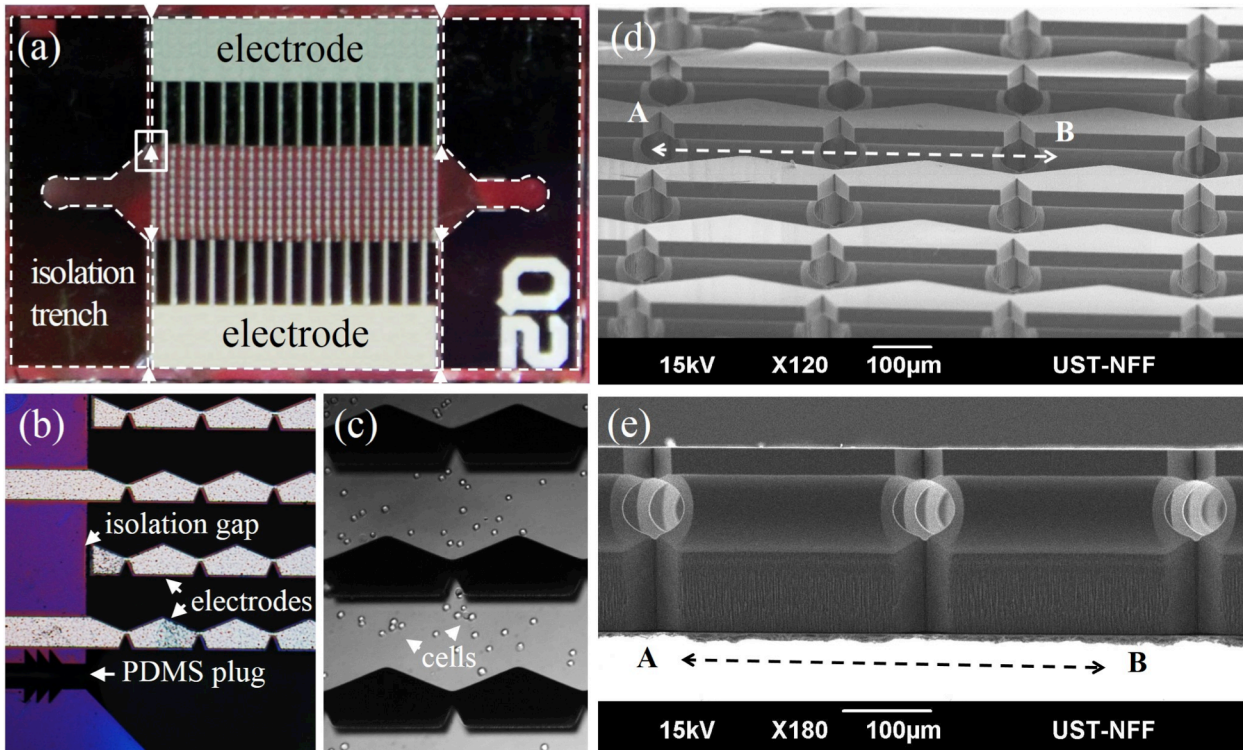

Fig. 2 (a) Representative device featuring a built-in transparent flow chamber between the interdigitated 3D comb array electrodes. The site denoted by the solid frame is further detailed (rotated 90°) in (b) revealing the characteristic segmented layout of the electrode digits arising from individual repeating units. (c) Cells imaged in the transparent device through DIC microscopy. (d) and (e) The fluidic pores formed by the castellated depth profiles of the adjacent units are further depicted in SEM images focusing on the 3D profile of the electrode digits from (d) oblique view and (e) cross-sectional view along the dashed line (AB-cut).

denote the cross-sectional planes crossing the co-axial pores (along path I) and the counter electrode units (along path II), respectively. Path II, since it sections convex corners of the electrodes, features field maxima and associated pDEP traps. From respective maps presented in upper as well as lower panels (path II), it is readily seen that these traps (denoted for a single electrode block "X") directly overlay stagnation points. Having the traps overlaid with stagnation points ensure that the cells held in place remain sheltered from excessive shear especially under increased flow rates for maximal throughput.

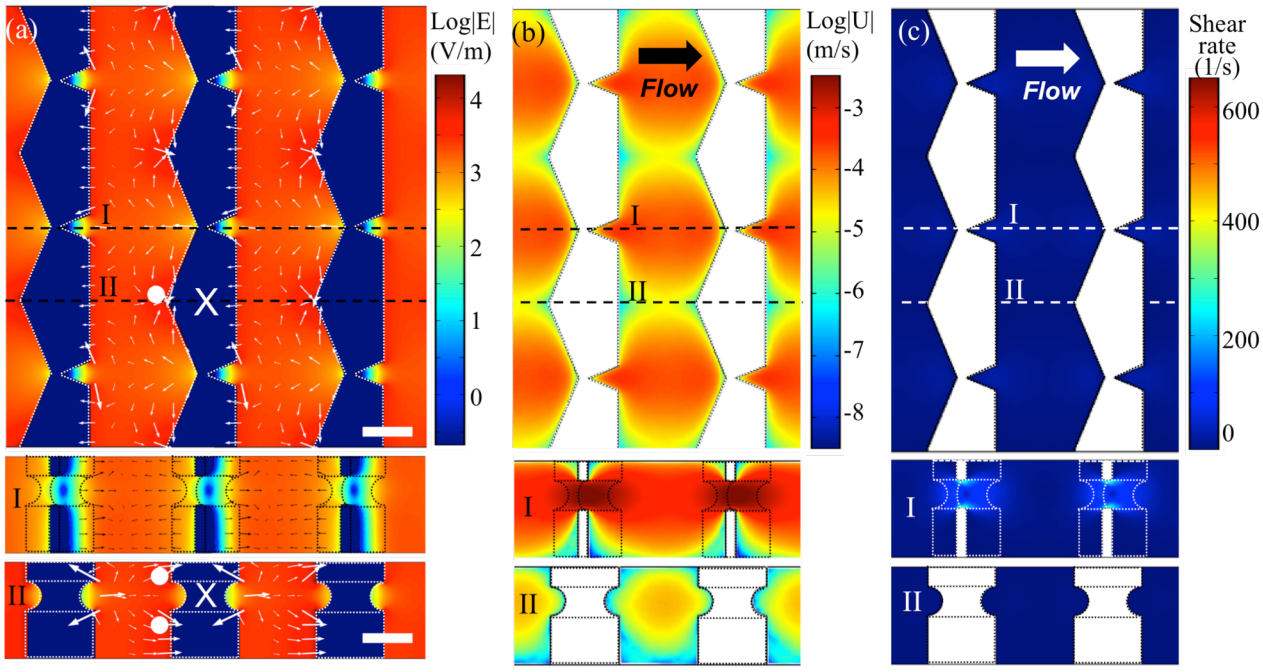

Fig. 3 (a) Electric field intensity maps with an overlay of DEP force vectors computed for a buffer conductivity of 100 μS/cm and an activation voltage of ±5 V_p at 400 kHz. Likely trapping sites for cells undergoing pDEP are denoted by the spheres placed near a single electrode segment ("X"). (b) Flow velocity and (c) shear rate distribution computed for an initial velocity of 116 μm/sec. Upper panel: maps of the device plane bisecting the top DRIE layer. The dashed lines mark the paths (I and II) along which the device cross-sectional maps are given in subsequent panels. Scale: 100 μm.

Throughout the device, cells are likely to be positioned around convex electrode corners away from the adjacent pores and near the chamber top and bottom as exemplified by solid spheres in Fig. 3a. For the simulated voltage level (±5 V_p at 400 kHz), the field strength within the traps gets as high as 10^4 V/m, which is far below the threshold for cell electropermeation (10^5 V/m)[54] and yet relatively strong to exert effective pDEP force to draw cells (compare field maps along paths I and II). Stagnant sites facing the downstream side of the electrode units are unlikely to draw cells, as doing so would require imparting a greater momentum change to cells passing by. Further, the field profiles near flat electrode edges are rather uniform and exert a considerably less effective force field than possible with those by convex electrode corners. Meanwhile, cells under nDEP would get repelled by the planar surfaces and carried by streams through the pores. Inside the pores, streams could reach up to a speed of ~1 mm/s, possibly exerting on cells a shear force ~ 400 1/s, yet briefly and far below the cell-lysis limit (~5000 1/s).[55]

DEP characteristics

To predict the response of cells to the applied field profile by castellated blocks at a given buffer conductivity, the field frequency dependence of the real part of the Clausius–Mossotti factor $\mathrm{Re}[f_{CM}(\omega)]$ has to be evaluated. By applying the single-shell dielectric model (ESI), the values of $\mathrm{Re}[f_{CM}(\omega)]$ were calculated. Fig. 4a plots the calculated values as a function of frequency for viable and nonviable cells for three distinct conductivity values of the immersion buffer (17, 100, and 1000 µS/cm). According to the model, viable cells in a low conductivity buffer 100 µS/cm exhibit a first crossover frequency around 30 kHz, above which they respond in accordance with pDEP, at a nearly full strength ($\mathrm{Re}[f_{CM}(\omega)]$~1) between ~0.2 and ~8 MHz. The crossover frequency (30 kHz) agrees well with earlier reports using the same cell type in a similarly low-conductivity buffer.[56] Further lowering the buffer conductivity to 17 µS/cm does not alter the profile but shifts the crossover frequency to 6 kHz. In contrast, increasing the buffer conductivity to 1000 µS/cm not only raises the crossover frequency to 300 kHz but also limits the pDEP force to ~60% of full capacity.

The dielectric model suggests that nonviable cells exhibit a relatively weak DEP response. This is expected since these cells are unable to preserve concentration gradient across their leaky membrane and fail to screen low-frequency fields. Particularly, those cells in high conductivity buffer (1000 µS/cm) are likely to express extremely weak nDEP ($\mathrm{Re}[f_{CM}(\omega)]\sim -0.05$) throughout the entire frequency spectrum. Those in low conductivity buffer, 17 µS/cm and 100 µS/cm, however, exhibit pDEP up to 100 kHz and 1 MHz, respectively. At higher frequencies, the polarity may change but the magnitude stays fairly weak.

The predictions of the model for viable and nonviable cells at the stated buffer conductivity values were independently confirmed in the device under stagnant conditions, Figs. 4b and c. Live cells exhibited nDEP at low frequencies while pDEP at high frequencies, Fig. 4b, with their crossover points increasing with the buffer conductivity as predicted by the model. The crossover frequencies were also found within the ranges given by the model. Nonviable cells at low buffer conductivities 17 and 100

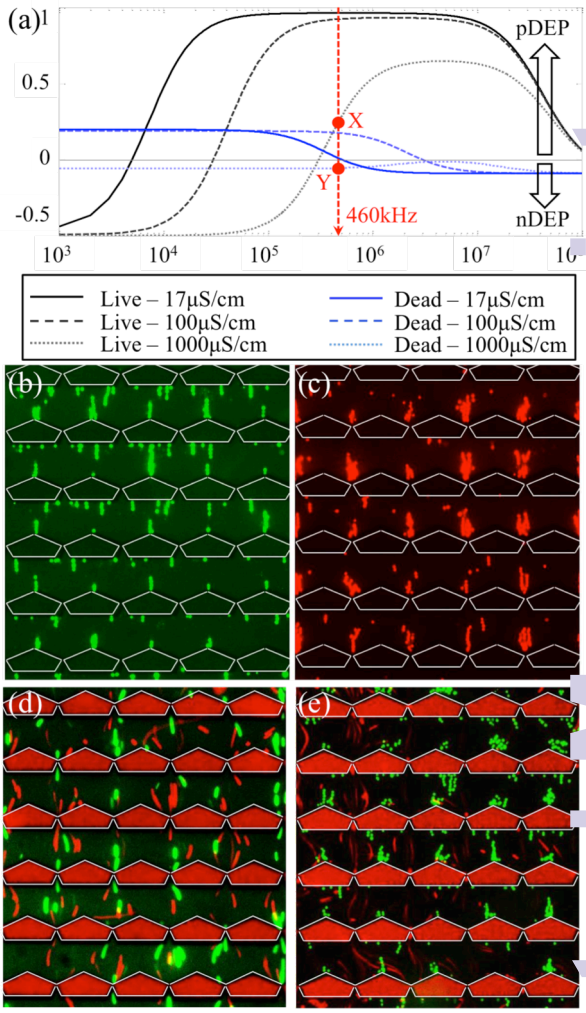

Fig. 4 (a) Plot of $\mathrm{Re}[f_{CM}(\omega)]$ based on the single-shell dielectric model for viable and nonviable cells at the stated buffer conductivity values (legend). The straight dashed line (vertical) and intersection points X (viable cells) and Y (nonviable cells) mark the field frequency and respective scaling factors for the DEP force vectors in the subsequent images. (b–e) Still images showing a section of the flow chamber: (b,c) under an activation voltage at ±10 V_p 460 kHz and stagnant flow conditions with (b) viable cells (green) and (c) nonviable cells (red) expressing pDEP and nDEP, respectively; (d,e) viable and nonviable cells transported from top to bottom in a pressure driven flow at 0.2 mL/h shown (d) before and (e) 5 s after the onset of voltage at ±15 V_p 460 kHz. Buffer: 1000 µS/cm.

µS/cm exhibited only pDEP across the entire frequency range up to 1 MHz. The behavior of nonviable cells at high conductivity buffer 1000 µS/cm could not be confirmed at low frequencies due to water electrolysis and the subsequent bubble formation. With the increased frequency, it became clear that nonviable cells exhibited weak nDEP, Fig. 4c. Electro-thermal effects (e.g. vortices) were not noticeable possibly owing to efficient heat removal by the 3D silicon digits. Computations suggested a maximum rise of 7 K under stagnant conditions for the higher voltage peak (±15 V_p). A lower thermal rise was noted with the flow rates experimented. Figs. 4d and e show viable and nonviable cells mixed together and applied at 0.2 mL/h (from top to bottom), depicted before and after the activation voltage onset, respectively. Viable cells (green) can be seen trapped accordi

to pDEP while nonviable cells (red) washed away as a result of nDEP (see Video S1, ESI).

In experiments, pore clogging was not encountered. Although some pores were found congested with nonviable cell aggregates, they continued to permeate. Cell aggregates occurred despite the measures taken against them (e.g., agitating cell suspensions gently through repeated pipetting). Measures were also taken against clogging (e.g., filtration of buffers, BSA passivation of the chamber). Clogging is likely to affect small pores whereas the pores featured here are sizeable enough and should accommodate most cell types. Large pores are also preferred to cut down backpressure, which was computed to be ~26 Pa at 0.2 mL/h. This pressure remains low despite two orders of magnitude rise over that of a fully open chamber without such 3D digits. Maximum attainable pore size while retaining a low electrical resistance between castellated blocks appears be no more than 120 μm and limited by the thickness of overall bulk silicon here.

Cell trajectories

Since the 3D comb array features castellated blocks, viable cells under pDEP exhibit distinctively unique trajectories. This can be seen through superimposed stills from time-lapse videos in Fig. 5a. The trajectories of single cells crossing a pair of digits under a fixed flow rate are depicted (0.1 mL/h). The cells follow the spreading streamlines as they emerge through the upstream digit and meet the downstream digit near a convex corner. Upon reaching the electrode in the absence of an activation voltage, the cell continues to advance, yet within the castellation and thus remains hidden under the silicon overhang until it reemerges through the pore (upper panel, Fig. 5a). However, when the digits are activated with a barely sufficient peak voltage (~2 V_p), the cell upon reaching the electrode gets lifted up to the level above that of the castellation and railed downstream by the electrode until the DEP force gets weaken and becomes ineffective (middle panel). The cell eventually descends into the castellation and then escapes through the pore. With a slightly stronger voltage peak (~3 V_p), the cell is pulled from the spreading streamlines under the influence of the DEP force toward the convex corner and directed to the trapping point by the upper electrode segment above the castellation (lower panel). Often, the DEP force vector exerted by such low activation falls short of pinning the cell at a point of first contact due to initial momentum of the cell; the cell slides downstream and decelerates to a point where the respective components of the DEP and drag force vectors ($\mathbf{F}_{DEP}$ and $\mathbf{F}_{drag}$) are balanced out. In the free-body diagram shown, this point is illustrated by a projection distance d, measured from the line that divides the electrode units.

Fig. 5b shows a plot of the shortest d registered in experiments for distinct voltage peaks and flow rates applied. Increasing the flow rate or reducing the voltage peak increases d in a linear fashion. That is, resting point shifts along the electrode edge closer to the upstream convex corner with an increased flow rate (the drag force) or a reduced voltage (the DEP force) to diminish the influence of strong drag while enhancing that of weak DEP. The shift appears to be more pronounced for variations of the voltage peak than for those of the flow rate simply because the DEP force is a quadratic function of the applied voltage whereas the drag force is linearly related to the velocity and rate of flow through a parallel plate fluidic chamber. The predictions slightly

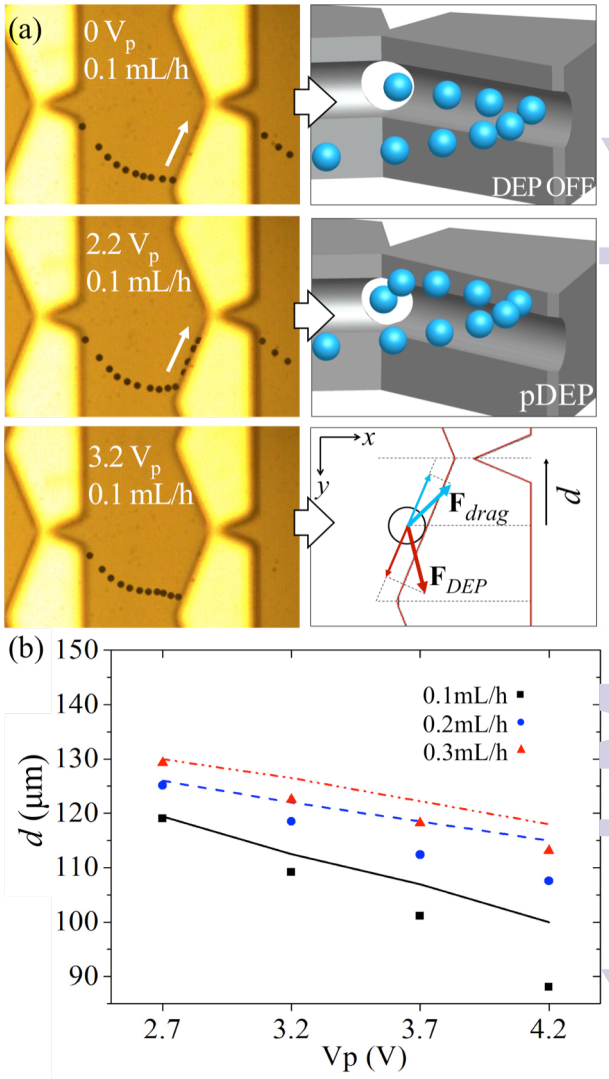

Fig. 5 (a) Typical cell trajectories revealed by superimposed images of single cells delivered at 0.1 mL/h in the absence and presence of voltage activation (400 kHz). 3D renderings illustrate cell trajectories in relation to the castellated surface profile for those cells that freely escape whereas free-body diagram denotes the force vectors for those cells being captured. (b) Plot of the peak voltage versus shortest d measured (as defined in free-body diagram) at a fixed flow rate (legend). The fittings are theoretical predictions at respective flows.

overestimate the measurements probably due to omission of the friction forces between the trapped cells and the electrode (ESI).

Live/dead cell separation

Subsequent experiments were performed to evaluate the utility of the 3D comb array for capturing viable cells while removing nonviable cells from a mixture (see Video S1, ESI). The live/dead cell mixture was suspended in high conductivity buffer (1000 μS/cm) since nonviable cells at such conductivity express very weak DEP (nDEP) and thus escape the field across the frequency range where viable cells experience strong pDEP. Experiments also included a cell mixture at a low buffer conductivity (100 μS/cm) so that viable cells could experience pDEP in full strength ($\mathrm{Re}[f_{CM}(\omega)]$~1) for effective trapping. Nonviable cells, under such conditions, however, also experience pDEP, albeit weak

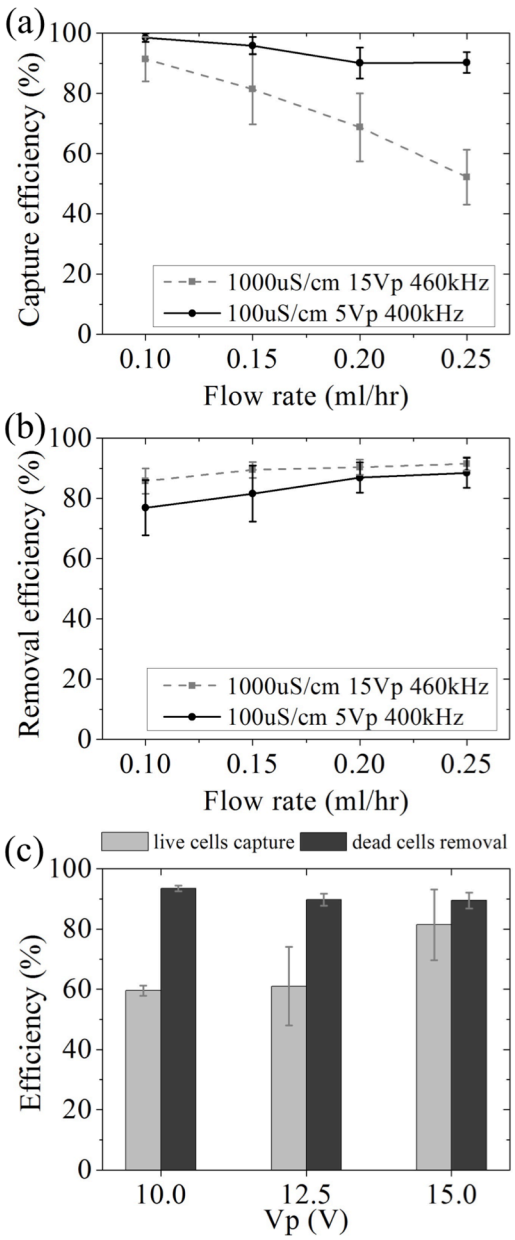

Fig. 6 Device efficiency plots as a function of (a) and (b) the flow rate and (c) the activation voltage. Efficiency of (a) capturing viable cells while (b) removing nonviable cells from a binary mixture at the stated buffer conductivity and activation voltage (legends). (c) Capture and removal efficiency against the peak voltage at 460 kHz (1000 μS/cm buffer and 0.15 mL/h flow). Data symbols and error bars denote mean ± s.d. ($n = 4$).

that might hamper their removal.

Fig. 6a compares the results obtained against various flow rates. Note that the sample in 100 μS/cm buffer was treated at a lower voltage (±5 V_p) and slightly lower frequency (400 kHz). Viable cells when introduced at 0.1 mL/h were captured with a comparably high efficiency (mean >90%) in either buffer although those in 1000 μS/cm buffer showed steady decline with increased flow, down to 52.2±9.1% corresponding to 0.25 mL/h. Viable cells in 100 μS/cm buffer maintained mean capture efficiency, despite a slight decline with increased flow, above 90% because of strong pDEP. The removal of nonviable cells in 1000 μS/cm buffer, in contrast, had no notable flow dependence, owing to weak nDEP, and stayed slightly below 90%, Fig. 6b. Those in 100 μS/cm buffer experienced pDEP, albeit weak, and were accordingly removed at a lower rate of 76.9±9.2% which corresponds to 0.1 mL/h. However, their removal rate at 0.25 mL/h was comparable to those in 1000 μS/cm buffer. The influence of the activation voltage on the capture and removal rates was also shown in Fig. 6c. While the removal rate was found independent of the activation voltage, the capture rate showed voltage dependence around ±15 V_p under the tested conditions (1000 μS/cm buffer and 0.15 mL/h flow).

Conclusion

In conclusion, we have introduced 3D silicon electrodes featuring castellated blocks and demonstrated their utility as building blocks in the construction of a unique interdigitated comb array. The array, despite its intricate structure consisting of monolithic electrodes and built-in fluidic pores that arise from castellated profiles, offers simplicity in electrical and fluidic integration through a self-aligned etching process, requiring neither multilayer lithography nor layer-to-layer alignment. We have characterized the array for the isolation of live/dead cells, taking advantage of effective field gradients and dielectrophoretic forces generated not only within its layout plane but also across its depth owing to the special surface profile. This characteristic, which is unlike of those with traditional volumetric electrodes featuring planar surfaces, has further facilitated trapping cells near stagnation points for enhanced viability and efficiency. Moreover, the trapping sites also coincide with stagnation points across the array layout plane, and yet encounter cells locally due to spreading streamlines exiting the pores under the flow-pinching effect and bringing cells nearby. In return, we have achieved a high rate of ~90% for both capturing viable cells and removing nonviable cells from their mixture by applying an activation voltage as low as ±5 V_p while handling a relatively large number of cells (10^5 cells per hour). The 3D electrodes with castellated blocks could pave the way to future designs where the electric field gradient and hydrodynamic flow profile can be coupled in ways that are further beneficial to cell separation and yet may not be trivial with traditional electrodes.

Acknowledgements

The authors thank Professor Randy Y. C. Poon of HKUST for providing HCT116 cell lines. This work was supported by the Research Grant Council of Hong Kong under Grant GRF621711.

Notes and references

[a] *Department of Electronic and Computer Engineering, Hong Kong University of Science and Technology, Clear Water Bay, Hong Kong, SAR, China. Fax: +852 2358 7068; Tel: +852 2358 1485; E-mail: eelyobas@ust.hk*

† Electronic Supplementary Information (ESI) available: [details of any supplementary information available should be included here]. See DOI: 10.1039/b000000x/

‡ Footnotes should appear here. These might include comments relevant to but not central to the matter under discussion, limited experimental and spectral data, and crystallographic data.

1 H. A. Pohl, Dielectrophoresis: *The behavior of neutral matter in nonuniform electric fields*, Cambridge University Press, Cambridge, 1978.

2 R. Pethig, *Biomicrofluidics*, 2010, **4**, 022811.
3 J. Voldman, *Annu. Rev. Biomed. Eng.*, 2006, **8**, 425-454.
4 K. Khoshmanesh, S. Nahavandi, S. Baratchi, A. Mitchell and K. Kalantar-zadeh, *Biosens. Bioelectron.*, 2011, **26**, 1800-1814.
5 B. Cetin and D. Q. Li, *Electrophoresis*, 2011, **32**, 2410-2427.
6 M. S. Pommer, Y. T. Zhang, N. Keerthi, D. Chen, J. A. Thomson, C. D. Meinhart and H. T. Soh, *Electrophoresis*, 2008, **29**, 1213-1218.
7 J. Cheng, E. L. Sheldon, L. Wu, M. J. Heller and J. P. O'Connell, *Anal. Chem.*, 1998, **70**, 2321-2326.
8 Y. Huang, S. Joo, M. Duhon, M. Heller, B. Wallace and X. Xu, *Anal. Chem.*, 2002, **74**, 3362-3371.
9 M. Stephens, M. S. Talary, R. Pethig, A. K. Burnett and K. I. Mills, *Bone Marrow Transpl.*, 1996, **18**, 777-782.
10 B. Cetin, Y. Kang, Z. M. Wu and D. Q. Li, *Electrophoresis*, 2009, **30**, 766-772.
11 G. H. Markx, M. S. Talary and R. Pethig, *J. Biotechnol.*, 1994, **32**, 29-37.
12 C. H. Tai, S. K. Hsiung, C. Y. Chen, M. L. Tsai and G. B. Lee, *Biomed. Microdevices*, 2007, **9**, 533-543.
13 K. Khoshmanesh, S. Baratchi, F. J. Tovar-Lopez, S. Nahavandi, D. Wlodkowic, A. Mitchell and K. Kalantar-zadeh, *Microfluid. Nanofluid.*, 2012, **12**, 597-606.
14 G. H. Markx, Y. Huang, X. F. Zhou and R. Pethig, *Microbiol.-UK*, 1994, **140**, 585-591.
15 H. Morgan, M. P. Hughes and N. G. Green, *Biophys. J.*, 1999, **77**, 516-525.
16 J. An, J. Lee, S. H. Lee, J. Park and B. Kim, *Anal. Bioanal. Chem.*, 2009, **394**, 801-809.
17 M. Uppalapati, Y. M. Huang, T. N. Jackson and W. O. Hancock, *Small*, 2008, **4**, 1371-1381.
18 P. Gascoyne, J. Satayavivad and M. Ruchirawat, *Acta Trop.*, 2004, **89**, 357-369.
19 U. Lei, C. W. Huang, J. Chen, C. Y. Yang, Y. J. Lo, A. Wo, C. F. Chen and T. W. Fung, *Lab Chip*, 2009, **9**, 1349-1356.
20 K. Cheung, S. Gawad and P. Renaud, *Cytom. Part A*, 2005, **65A**, 124-132.
21 J. Yang, Y. Huang, X. J. Wang, X. B. Wang, F. F. Becker and P. R. C. Gascoyne, *Biophys. J.*, 1999, **76**, 3307-3314.
22 P. R. C. Gascoyne and J. V. Vykoukal, *Proc. IEEE*, 2004, **92**, 22-42.
23 C. Kuttel, E. Nascimento, N. Demierre, T. Silva, T. Braschler, P. Renaud and A. G. Oliva, *Acta Trop.*, 2007, **102**, 63-68.
24 M. Cristofanilli, G. De Gasperis, L. S. Zhang, M. C. Hung, P. R. C. Gascoyne and G. N. Hortobagyi, *Clin. Cancer Res.*, 2002, **8**, 615-619.
25 Y. Hubner, K. F. Hoettges, G. E. N. Kass, S. L. Ogin and M. P. Hughes, *IEE Proc.: Nanobiotechnol.*, 2005, **152**, 150-154.
26 F. H. Labeed, H. M. Coley, H. Thomas and M. P. Hughes, *Biophys. J.*, 2003, **85**, 2028-2034.
27 Y. Huang, X. B. Wang, P. R. C. Gascoyne and F. F. Becker, *Biochim. Biophys. Acta, Biomembr.*, 1999, **1417**, 51-62.
28 K. Khoshmanesh, J. Akagi, S. Nahavandi, J. Skommer, S. Baratchi, J. M. Cooper, K. Kalantar-Zadeh, D. E. Williams and D. Wlodkowic, *Anal. Chem.*, 2011, **83**, 2133-2144.
29 R. Pethig and M. S. Talary, *IET Nanobiotechnol.*, 2007, **1**, 2-9.
30 X. J. Wang, F. F. Becker and P. R. C. Gascoyne, *Biochim. Biophys. Acta, Biomembr.*, 2002, **1564**, 412-420.
31 B. M. Taff and J. Voldman, *Anal. Chem.*, 2005, **77**, 7976-7983.
32 J. R. Kovac and J. Voldman, *Anal. Chem.*, 2007, **79**, 9321-9330.
33 T. Murata, T. Yasukawa, H. Shiku and T. Matsue, *Biosens. Bioelectron.*, 2009, **25**, 913-919.
34 Y. C. Xu, H. F. Yao, L. Wang, W. L. Xing and J. Cheng, *Lab Chip*, 2011, **11**, 2417-2423.
35 R. Pethig, Y. Huang, X. B. Wang and J. P. H. Burt, *J. Phys. D Appl. Phys.*, 1992, **25**, 881-888.
36 G. H. Markx and R. Pethig, *Biotechnol. Bioeng.*, 1995, **45**, 337-343.
37 Y. Huang, X. B. Wang, F. F. Becker and P. R. C. Gascoyne, *Biophys. J.*, 1997, **73**, 1118-1129.
38 X. B. Wang, J. Vykoukal, F. F. Becker and P. R. C. Gascoyne, *Biophys. J.*, 1998, **74**, 2689-2701.
39 S. Fiedler, S. G. Shirley, T. Schnelle and G. Fuhr, *Anal. Chem.*, 1998, **70**, 1909-1915.
40 M. Durr, J. Kentsch, T. Muller, T. Schnelle and M. Stelzle, *Electrophoresis*, 2003, **24**, 722-731.
41 C. H. Yu, J. Vykoukal, D. M. Vykoukal, J. A. Schwartz, L. Shi and P. R. C. Gascoyne, *J. Microelectromech. Sys.*, 2005, **14**, 480-487.
42 J. Park, B. Kim, S. K. Choi, S. Hong, S. H. Lee and K. I. Lee, *Lab Chip*, 2005, **5**, 1264-1270.
43 C. Iliescu, G. L. Xu, V. Samper and F. E. H. Tay, *J. Micromech. Microeng.*, 2005, **15**, 494-500.
44 C. Iliescu, L. M. Yu, G. L. Xu and F. E. H. Tay, *J. Microelectromech. Sys.*, 2006, **15**, 1506-1513.
45 L. S. Wang, L. Flanagan and A. P. Lee, *J. Microelectromech. Sys.*, 2007, **16**, 454-461.
46 L. Wang, L. A. Flanagan, N. L. Jeon, E. Monuki and A. P. Lee, *Lab Chip*, 2007, **7**, 1114-1120.
47 R. Martinez-Duarte, R. A. Gorkin, K. Abi-Samra and M. J. Madou, *Lab Chip*, 2010, **10**, 1030-1043.
48 M. Nasabi, F. J. Tovar-Lopez, K. Khoshmanesh, G. Kostovski and A. Mitchell, *J. Mater. Chem. C*, 2013, **1**, 401-405.
49 M. Nasabi, K. Khoshmanesh, F. J. Tovar-Lopez, K. Kalantar-zadeh and A. Mitchell, *Electrophoresis,* 2013, **34**, 3150–3154.
50 B. J. Kirby, *Micro- and Nanoscale Fluid Mechanics: Transport in Microfluidic Devices*, Cambridge University Press, New York, 2010.
51 X. X. Xing, M. Y. Zhang and L. Yobas, *J. Microelectromech. Sys.*, 2013, **22**, 363-371.
52 L. Yobas, R. K. Sharma, R. Nagarajan, V. D. Samper and P. S. R. Naidu, *J. Micromech. Microeng.*, 2005, **15**, 386-393.
53 L. Yobas, S. Martens, W. L. Ong and N. Ranganathan, *Lab Chip*, 2006, **6**, 1073-1079.
54 S. K. Kim, J. Y. Kim, K. P. Kim and T. D. Chung, *Anal. Chem.*, 2007, **79**, 7761-7766.
55 A. Salmanzadeh, L. Romero, H. Shafiee, R. C. Gallo-Villanueva, M. A. Stremler, S. D. Cramer and R. V. Davalos, *Lab Chip*, 2012, **12**, 182-189.
56 S. Shim, K. Stemke-Hale, J. Noshari, F. F. Becker and P. R. C. Gascoyne, *Biomicrofluidics*, 2013, **7**, 011808.